PROCEEDINGS OF SCIENCE

Isovector Axial Charge and Form Factors of Nucleons from Lattice QCD

Rajan Gupta[a,*]

[a] *Los Alamos National Laboratory, Theoretical Division T-2, Los Alamos, NM 87545, USA*

E-mail: rajan@lanl.gov

I present an overview of the calculations of the isovector axial vector form factor of the nucleon, $G_A(Q^2)$, using lattice QCD. Based on a comparison of results from various collaborations, a case is made that lattice results are now consistent within 10%. A similar level of uncertainty is found also in the axial charge g_A^{u-d}, the mean squared axial charge radius, $\langle r_A^2 \rangle$, the induced pseudoscalar charge g_P^*, and the pion-nucleon coupling $g_{\pi NN}$. These lattice results for $G_A(Q^2)$ are already compatible with those obtained from the recent MINERνA experiment but lie 2-3σ higher than the phenomenological extraction from the old ν-deuterium bubble chamber scattering data for $Q^2 > 0.3$ GeV^2. Fits to our data show that the dipole ansatz does not have enough parameters to parameterize the form factor over the range $0 \le Q^2 \le 1$ GeV^2, whereas even a z^2 truncation of the z-expansion or a low order Padé are sufficient. Looking ahead, lattice QCD calculations will provide increasingly precise results over the range $0 \le Q^2 \lesssim 1$ GeV^2, and MINERνA-like experiments will extend the range to $Q^2 \sim 2$ GeV^2 or higher. To increase precision of lattice data to the percent level, new developments are needed to address two related issues: the exponentially falling signal-to-noise ratio in all nucleon correlation functions and removing excited state contributions. Nevertheless, even with the current methodology, significant reduction in errors is expected over the next few years with higher statistics data on more ensembles closer to the physical point.

The 40th International Symposium on Lattice Field Theory (LATTICE2023)
July 31st - August 4th, 2023
Fermi National Accelerator Laboratory

*Speaker

PoS(LATTICE2023)124

1. Introduction

The axial charge, g_A^{u-d}, gives the strength of the coupling of the weak current to the nucleons. It has been determined very accurately from the asymmetry parameter A (relative to the plane defined by the directions of the neutron spin and the emitted electron) in the decay distribution of the neutron, $n \to p + e^- + \overline{\nu}_e$. The best determination of the ratio of the axial to the vector charge, g_A/g_V, comes from using (i) polarized ultracold neutrons (UCN) by the UCNA collaboration, 1.2772(20) [1, 2], and (ii) cold neutron beam by PERKEO III, 1.27641(45)(33) [3, 4]. Note that, in the SM, $g_V = 1$ up to second order corrections in isospin breaking [5, 6] as a result of the conservation of the vector current.

The axial charge enters in many analyses of nucleon structure, of the Standard Model (SM), and in probes of beyond-the-SM (BSM) physics [7, 8]. For example, it enters in the relation between the Cabibbo-Kobayashi-Maskawa (CKM) matrix element V_{ud} and the neutron lifetime, τ_n. High precision extraction of V_{ud}, knowing τ_n and g_A, is important for the test of the unitarity of the first row of the CKM matrix [9–11]. It is needed in the analysis of neutrinoless double-beta decay [12] and in the rate of proton-proton fusion [13], the first step in the thermonuclear reaction chains that power low-mass hydrogen-burning stars like the sun.

The axial-vector form factor (AVFF) gives the dependence of this coupling on the momentum squared transferred by the weak current to the nucleon. It is an input in the theoretical calculation of the neutrino-nuclei scattering cross-section needed for the analysis of neutrino oscillation experiments [14–16]. The cleanest experimental measurement would be from scattering neutrinos off liquid hydrogen targets, however, these are not being carried out due to safety concerns. Extractions from ongoing neutrino scattering experiments (T2K, NOvA, MINERvA, MicroBooNE, SBN) have uncertainty due to those in the cross-section and the incoming flux, and from the lack of precise reconstruction of the final state of the struck nucleus. Conversely, uncertainty in the AVFF feeds into the uncertainty in the incoming neutrino energy that is needed to determine the oscillation parameters.

The MINERνA experiment [17], using a separation based on kinematics, has recently extracted the axial-vector form factor of the nucleon from the charged current elastic scattering process $\overline{\nu}_\mu H \to \mu^+ n$ in which the free proton in the hydrogen (H) (part of the hydrocarbon in the target) gets converted into a neutron. This opens the door to direct measurements of the nucleon axial-vector form factor without the need for extraction from scattering off nuclei, whose analysis involves nuclear corrections that have unresolved systematics. On the theoretical front, lattice QCD provides the best method for first principal non-perturbative predictions with control over all sources of uncertainty [14, 15].

A recent comparison [18] of results for the AVFF from lattice QCD [19], the MINERνA experiment [17], and the phenomenological extraction from neutrino-deuterium data [20] showed that in the near term the best prospects for determining the AVFF will be a combination of lattice QCD calculations and MINERνA-like experiments. Lattice QCD will provide the best estimates for $Q^2 \lesssim 0.5$ GeV^2, and be competitive with MINERνA for $0.5 \lesssim Q^2 \lesssim 1$ GeV^2. For $Q^2 \gtrsim 1$ GeV^2, new ideas are needed for robust predictions using lattice QCD.

The goal of theory efforts in support of neutrino oscillation experiments is robust calculations of the cross-section for targets, such as ^{12}C, ^{16}O, and ^{40}Ar, being used in experiments. This involves a four step process: a precise determination of the AVFF, nuclear models of the ground state of

the nuclei from which the neutrino scatters, the intra-nucleus evolution of the struck nucleon using many-body theory to include complex nuclear effects up to ≈ 5 GeV for the DUNE experiment, and the evolution of the final state particles to the detectors. The overall program requires complete implementation of these within Monte Carlo neutrino event Generators [14–16] with full uncertainty quantification in each step. The output of the generators is the essential input required by experimentalists for determining neutrino oscillation parameters from current and future experiments.

Here I review the status of lattice QCD calculations of the axial charge, g_A^{u-d} and the AVFF. In addition, note that the flavor diagonal axial charges $g_A^{u,d,s,c,b}$ provide the contribution of each quark flavor to the spin of the nucleon, whose calculation is computationally more expensive due to the additional disconnected contributions. Current status of results for these nucleon charges has been reviewed by the Flavor Lattice Averaging Group (FLAG) in 2019 and 2021 [21, 22]). Including results post FLAG 2021 [23–27], the values from the various calculations with 2+1- and 2+1+1-flavors of sea quarks lie in the ranges $1.22 \lesssim g_A^{u-d} \lesssim 1.32$, $0.74 \lesssim g_A^{u} \lesssim 0.89$, $-0.48 \lesssim g_A^{d} \lesssim -0.38$, and $-0.06 \lesssim g_A^{s} \lesssim -0.025$. There have been no substantial new results for flavor diagonal charges since the FLAG reports, so I will not discuss them further in this work.

Based on the results in Refs. [19, 23, 26–29], I present the case that lattice results for AVFF over the range $0 < Q^2 \leq 1$ GeV^2 are also available with $\lesssim 10\%$ uncertainty and agree with MINERνA results to within a combined sigma as discussed in Ref. [18] but disagree with the neutrino-deuterium results for $Q^2 > 0.3$ GeV^2. At the same time, I also highlight the need for much higher statistics and better control over excited state contributions to nucleon correlators in lattice calculations for the uncertainty to be reduced to the percent level.

The outline of this review is as follows. I will summarize the methodology and steps in the calculation of the axial and pseudoscalar form factors in Sec. 2. This includes a discussion of the nucleon 3-point correlation functions calculated in Sec. 2.1, removing possible excited state contributions (ESC) in Sec. 2.2, and how form factors are then obtained from them in Sec. 2.3. I then review the operator constraint imposed on the three form factors, the axial, $G_A(Q^2)$, the induced pseudoscalar, $\widetilde{G}_P(Q^2)$, and the pesudoscalar $G_P(Q^2)$ by the axial Ward-Takahashi (also referred to in literature as the partially conserved axial current (PCAC)) identity in Sec. 2.4, and how it provides a data driven method for validating the enhanced contributions of multihadron, $N\pi$, excited states. These enhanced excited state contributions are due to the coupling of the axial and pseudoscalar currents to a pion, i.e., the pion pole dominance hypothesis. Extrapolation of the lattice results to the physical point defined by the continuum ($a = 0$) and infinite volume ($M_\pi L \to \infty$) limits at physical light quark masses in the isospin symmetric limit, i.e., $m_u = m_d$ set using the neutral pion mass ($M_{\pi^0} = 135$ MeV) is discussed in Sec. 2.5. A consistency check on the extraction of the axial charge is discussed in Sec. 2.6. I will then review the results for the AVFF obtained by the various lattice collaborations after extrapolation to the physical point in Sec. 3, and the comparison of lattice QCD result, the recent MINERνA data, and the phenomenological extraction from the old neutrino-deuterium scattering data along with my perspective on future improvements in Sec. 4. The concluding remarks are given in Sec. 5.

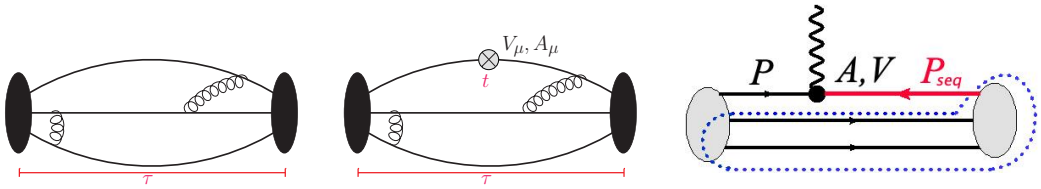

Figure 1: Quark line diagrams for the gauge invariant time-ordered correlation functions $C^{2pt}(\boldsymbol{p};\tau)$ and $C^{3pt}_J(\boldsymbol{q};t,\tau)$. The gluon lines are shown only to indicate that all possible gluon exchanges between quarks are included, i.e., it is a fully non-perturbative calculation. The electromagnetic and axial form factors are calculated by inserting the vector, V_μ, and axial, A_μ, currents, respectively, with momentum $\mathbf{q}$ at times t in between the nucleon source and sink separated by time τ. The construction of the source for the sequential propagator $P_{\rm seq}$ is shown schematically in the right panel. The two lower quark lines within the dotted region are tied at the sink by $\mathcal{N}$, leaving the spin and color indices of the third spinor to serve as the source.

2. Calculation of the axial vector form factors using lattice QCD

The quark line diagrams for the 2-point, C^{2pt} and the 3-point $C^{3pt}_J(\boldsymbol{q};t,\tau)$ (with the insertion of the axial, A_μ, (or vector V_μ) and pseudoscalar, P, currents) correlators are shown in Fig. 1. The methodology for calculating these is the same in all ongoing calculations. For $C^{3pt}_J(\boldsymbol{q};t,\tau)$, two kinds of quark propagators are calculated by solving, using Krylov solvers such as conjugate gradient and accelerated using multigrid [30], the linear equation $DP = \eta$ where D is the Dirac matrix on the lattice and η is a source vector. The first, P, is constructed using a delta function or smeared η and shown moving forward from the source location, i.e., from the left blob in the right panel in Fig. 1. The second is a sequential propagator, $P_{\rm seq}$, shown moving backwards (red line from the right blob representing the sink) from $\eta = nucleon$ source with definite momentum $\mathbf{p}_f$. This *nucleon* source, shown schematically by the part of the diagram lying inside the dotted area, is constructed by contracting together two original (P) propagators. The insertion of the current with 3-momentum $\mathbf{q}$ between the source and sink nucleons then reduces to that between the original propagator and the sequential propagator, again shown schematically by the top line. By momentum conservation, the source nucleon is then projected to momentum $\mathbf{p}_i = \mathbf{p}_f - \mathbf{q}$. The Euclidean 4-momentum transfer squared is given by $Q^2 = \mathbf{q}^2 - (E_N - M_N)^2$.

In current calculations (the standard method) the nucleon interpolating operator, $\mathcal{N}$, used is

$$\mathcal{N}(x) = \epsilon^{abc}\left[q_1^{aT}(x) C\gamma_5 \frac{1\pm\gamma_4}{2} q_2^b(x)\right] q_1^c(x)\,, \tag{1}$$

where $C = \gamma_4\gamma_2$ and the optional factor $1 \pm \gamma_4$ projects on to positive parity nucleon states propagating forward/backward in time for zero momentum correlators. Developing a variational basis of interpolating operators that includes all states making significant contributions, including $N\pi$ states, i.e., the holy grail of taming ESC, is still work under progress [31, 32].

A short description of the six steps in the calculation of the AVFF that are common to all fermion discretization schemes and independent of the selection of input simulation parameters is given next in Secs. 2.1–2.6.

2.1 Correlation functions C^{2pt} and $C^{3pt}_J(\mathbf{q};t,\tau)$

Two kinds of smeared sources, η, have been used to generate the original and sequential quark propagators in most lattice calculations: (i) Wuppertal [33] and (ii) exponential source [25]. The quark propagators so obtained are stitched together to construct the gauge invariant time-ordered correlation functions $C^{2pt}(\boldsymbol{p};\tau)$ and $C^{3pt}_J(\boldsymbol{q};t,\tau)$ shown in Fig. 1, whose spectral decompositions are

$$C^{2pt}(\boldsymbol{p};\tau) \equiv \langle\Omega|\mathcal{T}(\mathcal{N}(\tau)\overline{\mathcal{N}}(0))|\Omega\rangle = \sum_{i=0} |A'_i|^2 e^{-E_i\tau}\,, \tag{2}$$

$$C^{3pt}_J(\boldsymbol{q};t,\tau) \equiv \langle\Omega|\mathcal{T}(\mathcal{N}(\tau)J_\Gamma(t)\overline{\mathcal{N}}(0))|\Omega\rangle = \sum_{i,j=0} A'_i A^*_j \langle j|J_\Gamma|i'\rangle e^{-E_i t - M_j(\tau-t)}\,, \tag{3}$$

where $J_\Gamma = A_\mu = \overline{\psi}\gamma_\mu\gamma_5\psi$ or $J_\Gamma = P = \overline{\psi}\gamma_5\psi$ is the quark bilinear current inserted at time t with momentum $\boldsymbol{q}$, and $|\Omega\rangle$ is the vacuum state. In the $C^{3pt}_J(\boldsymbol{q};t,\tau)$, using the quantum mechanical right to left time ordering, the nucleon in the final state $\langle j|$ is, by construction, projected to zero momentum, i.e., $p_j = (M,\mathbf{0})$, whereas the initial state $|i'\rangle$ is projected onto definite momentum $p_i = (E,\boldsymbol{p})$ with $\boldsymbol{p} = -\boldsymbol{q}$ by momentum conservation. The prime in $|i'\rangle$ indicates that this state can have non-zero momentum. Consequently, the states on the two sides of the inserted operator J are different for all $\mathbf{q} \neq 0$. The goal is to extract the ground-state matrix elements (GSME), $\langle 0|J|0'\rangle$, from fits to Eq. (3).

A major challenge in the analysis of all nucleon correlators is the exponential decay of the signal-to-noise ratio, i.e., as $e^{-(M_N - 1.5M_\pi)\tau}$ with the source-sink separation τ [34, 35]. With ($O(10^5)$ measurements), a good signal in $C^{2pt}(\boldsymbol{p};\tau)$ and $C^{3pt}_J(\boldsymbol{q};t,\tau)$ extends to ≈ 2 and ≈ 1.5 fm, respectively.

At these τ, the residual contribution of many theoretically allowed radial and multihadron excited states are observed to be significant. These states arise because the standard nucleon interpolating operator $\mathcal{N}$, defined in Eq. (1) and used to construct the correlation functions given in Eqs. (2) and (3), couples to a nucleon and all its excitations with positive parity including multihadron states, the lowest of which are $N(\mathbf{p})\pi(-\mathbf{p})$ with $|\mathbf{p}_{\rm lowest}| = 2\pi/La$ and $N(\mathbf{0})\pi(\mathbf{0})\pi(\mathbf{0})$. Since it is not known, *a priori*, which excited states contribute significantly to a given $C^{3pt}_J(\boldsymbol{q};t,\tau)$, the first goal is to develop methods to identify these and remove their contributions. Operationally this boils down to knowing/determining the energies E_i to put in fits to data using the theoretically rigorous (for unitary actions) spectral decomposition given in Eq. (3). Note that the A_i are not needed as they come in combinations $A'_i A^*_j \langle j|J_\Gamma|i'\rangle$, which are fit parameters and never used.

2.2 Extracting the ground state matrix elements: exposing and incorporating $N\pi$ states

The most direct way to extract $\langle 0|J|0'\rangle$ is to make fits to Eq. (3) keeping as many intermediate states as allowed by data's precision and demonstrate convergence. The problem is that even unconstrained 2-state fits are numerically ill-posed. The next option is to take the E_i from $C^{2pt}(\boldsymbol{p};\tau)$ as $\mathcal{N}$ creates the same set of states in C^{2pt} and C^{3pt}_J and input these in fits to $C^{3pt}_J(\boldsymbol{q};t,\tau)$, either by doing simultaneous fits or via priors within say a bootstrap process to correctly propagate the errors. Of these, the ground state A'_0, A_0, and E_0 are well-determined from fits to the 2-point function. Similarly, one would expect E_1 can also be taken from C^{2pt}. This was the strategy used until 2017 when it was shown in Ref. [36] that the resulting form factors do not satisfy the constraint imposed on them by PCAC. Deviations from PCAC due to discretization effects of about $\approx 5\%$ were expected, however, almost a factor of two was found on the physical pion mass ensembles.

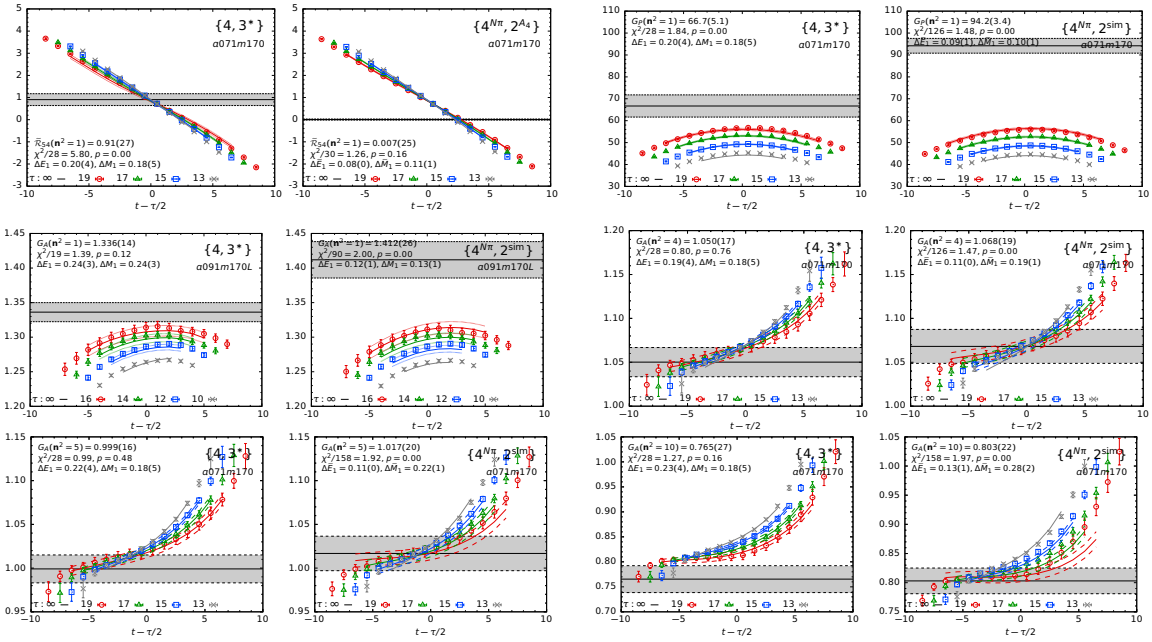

Figure 2: Data for the ratio $C_J^{3\text{pt}}(\boldsymbol{q},t,\tau)/\sqrt{C^{2\text{pt}}(\boldsymbol{q},t)C^{2\text{pt}}(0,\tau-t)}$ that, in the limits $(\tau-t)\to\infty$ and $t\to\infty$, should be independent of τ and t, i.e., lie on a horizontal line in the center about $t=\tau/2$ with value that is the GSME. Current data show large ESC, and the grey band is the estimate of GSME given by the fit to Eq. (3). In each row, the data in each pair of panels are the same but the fit on the left is without the $N\pi$ state and on the right is with. The top row (panels 1 and 2) show the data and fit to $J=A_4$ with $\boldsymbol{n}=(0,0,1)$. These two panels illustrate (i) the improvement (χ^2/dof) in the fit to $J=A_4$ data with the inclusion of the $N\pi$ state and (ii) a very large ESC indicated by the large slope slowly rotating counterclockwise to the expected horizontal band. The right two panels show the data and fits to $J=P$ with $\boldsymbol{n}=(1,0,0)$ that should give G_P. These two panels illustrate that the difference in G_P with and without including the $N\pi$ state is about 50% (enhanced ESC) and the χ^2/dof is better with the $N\pi$ state. Panels in rows two and three show the data and fit to $J=A_3$ with $\boldsymbol{n}=(1,0,0),\ (2,0,0),\ (2,1,0),\ (3,1,0)$ that should give G_A for $\tau\to\infty$. Each pair of panels illustrates that the difference in G_A with and without including the $N\pi$ state is a few percent and the χ^2/dof of the two fits is comparable. Note the change in the behavior: the $\boldsymbol{n}=(1,0,0)$ data converge from below, while for (1,1,1) and higher momenta, the data are rotating clockwise to the expected horizontal line. Also, the fits become less robust with increasing $\boldsymbol{n}$. See Ref. [27] for details on these data and the fits.

The reason was provided by Bär [37, 38] using χPT: enhanced contributions to ME from multihadron, $N\pi,\ldots$, excited states that have much smaller mass gaps than of radial excitations, the lowest being ≈ 1230 versus N(1440). These states were not evident in fits to $C^{2\text{pt}}(\boldsymbol{p};\tau)$ as they have small amplitudes. A different approach to analysis that includes the $N\pi$ states was needed.

It turned out that 2-state fits to $C^{3\text{pt}}_{A_4}$ exposed these states and provided a data-driven method [39]. These fits confirmed that the lowest of the tower of $N(\mathbf{p})\pi(-\mathbf{p})$ states makes a very significant contribution. By itself, $C^{3\text{pt}}_{A_4}$ is dominated by excited states and fits to it using the E_i from $C^{2\text{pt}}$ gave very poor χ^2/dof . Making fits leaving E_1 a free parameter dramatically improved the χ^2/dof (compare the left two panels in the top row of Fig. 2), and the resulting output values of E_1 on the $\mathbf{p}=0$ ($\mathbf{p}$) side of operator insertion were roughly consistent with $N(\mathbf{p}=1)\pi(\mathbf{p}=-1)$ ($N(0)\pi(\mathbf{p})$) as shown in Fig. 3 (left), reproduced from Ref. [39]. An illustration of the current understanding of the process giving GSME and of those involving the lowest excited states contributing is shown in

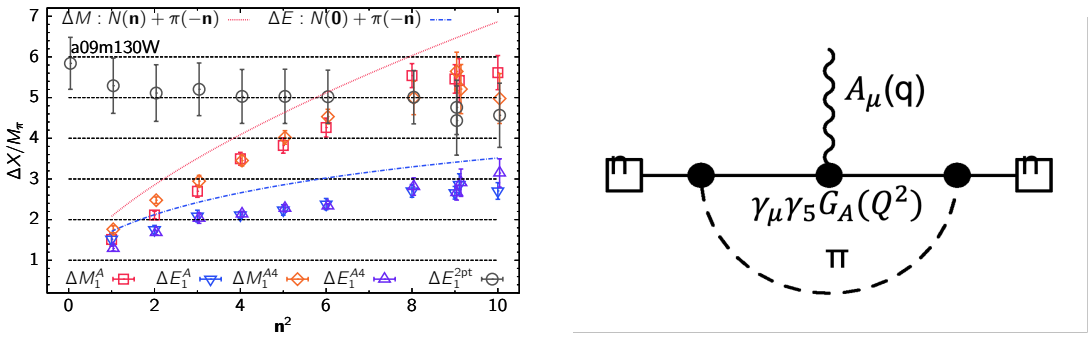

Figure 3: (Left) Results for the energy gaps, labeled ΔE_1^{A4} and ΔM_1^{A4}, for the first excited state extracted from fits to the C_{A_4} correlator. These mass gaps are compared with the first excited state energy ΔE_1^{2pt} from four-state fits to the nucleon two-point correlator. Note that the difference between them (black circles versus blue triangles), and consequently the difference between the form factors extracted increases as $M_\pi \to 135$ MeV and $\boldsymbol{n^2} \to 0$ (equivalently $Q^2 \to 0$). (Right) The 1-loop correction to the 3-point function in χPT.

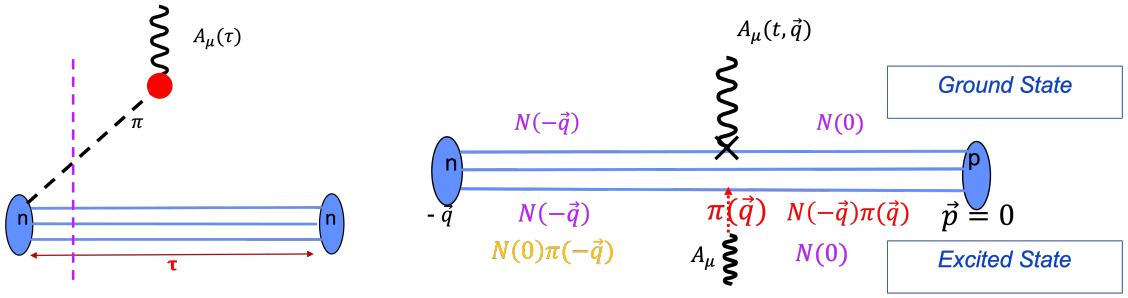

Figure 4: The quark line diagrams illustrating the contribution of $N\pi$ states. (Left) the current A_μ annihilates the pion produced by the source. (Right) The states involved in the transitions: the ground state process is shown above the quark line diagram and those involving an excited state on one side of the current insertion are shown below.

Fig. 4 (right). The caption of Fig. 2 points out some of the features of ESC observed in current data and the efficacy of fits to C_J^{3pt} with and without including the lowest $N\pi$ state to remove the ESC.

The fact that there is enhancement of ME in the axial channel has been understood for over 60 years as the "pion pole dominance" (PPD) hypothesis. On the lattice, the creation of a $N\pi$ state by $\mathcal{N}$ is suppressed by V, the 3-d volume, compared to just the nucleon as each state has a normalization factor of $1/V$ for a point (local) source $\mathcal{N}$. The axial current can, however, couple to this pion, and because the pion is light, this coupling can occur anywhere in the time slice at which the current is inserted with momentum $\boldsymbol{q}$ (see Fig. 4 (left)). This gives a factor of V enhancement, approximately cancelling the normalization factor $1/V$ [37, 38]. This enhanced contribution to the ME when the pion comes on-shell is an artifact that has to be removed. Note that since energy is not conserved on the lattice, both the neutron and the pion can come on shell, however, since momentum is conserved, possible excited states must have the same total momentum as the created neutron state. PPD tells us that the axial current with momentum $\boldsymbol{q}$ can be viewed as the insertion of a pion with $\boldsymbol{q}$, and this has a large coupling to the nucleon. These processes are illustrated in Fig. 4.

Having identified large contributions from the $N(\mathbf{p}=1)\pi(\mathbf{p}=-1)$ state, certainly in the extraction of $\widetilde{G}_P$ and G_P, the question is—do we need to include other multihadron and radial

excited state contributions if we want results with percent level precision? What about in G_A? Note that, in addition to the enhanced contribution shown in Fig. 4, χPT also indicates that the 1-loop contributions due to the diagram shown in Fig. 3 (right) (again a $N\pi$ contribution) could be $O(5\%)$ in all the five $C_J^{\rm 3pt}$. Thus the $N\pi$ state could also be significant for extracting G_A and the charge g_A (the GSME $\langle 0|A_3|0'\rangle$) from C_{A_3} at the percent precision desired. Based on these arguments, it is clear that one needs at least 3-state fits to the five $C_J^{\rm 3pt}$ in Eq. (3)—the ground state, the $N\pi$ state and the third that effectively accounts for all other excited state contributions.

In my evaluation, details of the fits made to remove ESC are the most significant differences between the calculations performed by the different collaborations. With the current methodology, higher statistics data are badly needed to improve these fits, i.e., include more states in the fits, and gradually reduce the dependence on exactly how the analyses are done.

A very important point to remember in such analyses is that fit parameters in a truncated ansatz (the A_i and E_i in say a 3-state fit in our case) try to incorporate the effects of all contributions. Thus the connection between parameters coming out of fits to a truncated Eq. (3) and physical states made in Figs. 3 and 4 is very approximate at best. Thus, when I write "$N\pi$ state" I really only mean an E_1 close to that of a non-interacting $N(1)\pi(-1)$ state and/or an $N(0)\pi(0)\pi(0)$ state that is essentially degenerate on our lattices.

2.3 Extracting the form factors

Once the GSME, $\langle 0|J|0'\rangle$, have been extracted, their Lorentz covariant decomposition into the axial G_A, induced pseudoscalar $\widetilde{G}_P$, and pseudoscalar G_P form factors is

$$\langle N(\boldsymbol{p}_f)|A_\mu(\boldsymbol{q})|N(\boldsymbol{p}_i)\rangle = \overline{u}(\boldsymbol{p}_f)\left[G_A(Q^2)\gamma_\mu\gamma_5 + q_\mu\gamma_5\frac{\widetilde{G}_P(Q^2)}{2M}\right]u(\boldsymbol{p}_i)\,, \tag{4}$$

$$\langle N(\boldsymbol{p}_f)|P(\boldsymbol{q})|N(\boldsymbol{p}_i)\rangle = \overline{u}(\boldsymbol{p}_f)\left[G_P(Q^2)\gamma_5\right]u(\boldsymbol{p}_i)\,, \tag{5}$$

where $u(\boldsymbol{p})$ is the nucleon spinor with momentum $\boldsymbol{p}$, $q = p_f - p_i$ is the momentum transferred by the current, $Q^2 = -q^2 = \boldsymbol{q}^2 - (E(\boldsymbol{p}_f) - E(\boldsymbol{p}_i))^2$ is the space-like four momentum squared transferred. On the lattice, the discrete momenta are $\boldsymbol{p} = 2\pi\boldsymbol{n}/La = 2\pi(n_x, n_y, n_z)/La$ with $n_i \in \pm\{0\ldots L\}$. The spinor normalization used is

$$\sum_s u(\boldsymbol{p}, s)\overline{u}(\boldsymbol{p}, s) = \frac{E(\boldsymbol{p})\gamma_4 - i\gamma\cdot\boldsymbol{p} + M}{2E(\boldsymbol{p})}\,. \tag{6}$$

It is important to note that the excited states have to be removed from the correlation functions,C, which have the spectral decomposition given in Eq. (3), and not from the form factors, i.e., after the decompositions. Eqs. (4) and (5) are only valid for GSME, i.e., $|N(\boldsymbol{p}_i)\rangle$ and $\langle N(\boldsymbol{p}_f)|$ are assumed to be ground states of the nucleon. If there are residual ESC, then additional "transition" form factors have to be included in the rhs of Eqs. (4) and (5).

Assuming GSME have been extracted, and choosing the nucleon spin projection to be in the

"3" direction, the explicit form of the decompositions in Eqs. (4) and (5) become

$$C_{A_{\{1,2\}}}(\boldsymbol{q}) \to K^{-1}\left[-q_{\{1,2\}}q_3\frac{\widetilde{G}_P}{2M}\right], \tag{7}$$

$$C_{A_3}(\boldsymbol{q}) \to K^{-1}\left[-q_3^2\frac{\widetilde{G}_P}{2M} + (M+E)G_A\right], \tag{8}$$

$$C_{A_4}(\boldsymbol{q}) \to K^{-1}q_3\left[(M-E)\frac{\widetilde{G}_P}{2M} + G_A\right], \tag{9}$$

$$C_P(\boldsymbol{q}) \to K^{-1}q_3 G_P\,, \tag{10}$$

where the kinematic factor $K \equiv \sqrt{2E(E+M)}$. In each case, data with all equivalent momenta that have the same $\boldsymbol{q}^2$ are averaged to improve the statistical signal. These correlation functions are complex valued, and the signal, for the CP symmetric theory, is in Im C_{A_i}, Re C_{A_4}, and Re C_P.

It is clear that G_P is determined uniquely from C_P (Eq. (10)), and for certain momenta $\widetilde{G}_P$ from $C_{A_{\{1,2\}}}$ using Eq. (7). The $C_{A_3}(\boldsymbol{q})$ and $C_{A_4}(\boldsymbol{q})$ give linear combinations of G_A and $\widetilde{G}_P$, and Eq. (8) gives only G_A when $q_3 = 0$.

2.4 Satisfying PCAC

The non-singlet PCAC relation between bare axial, $A_\mu(x)$, and pseudoscalar, $P(x)$, currents is:

$$\partial_\mu A_\mu = 2\widehat{m}P\,, \tag{11}$$

where the quark mass parameter $\widehat{m} \equiv Z_m m_{ud} Z_P Z_A^{-1}$ includes all the renormalization factors, and $m_{ud} = (m_u + m_d)/2 = m_l$ is the light quark mass in the isospin symmetric limit. Using the decomposition in Eqs. (4) and (5) of GSME, the PCAC relation requires that the three form factors G_A, $\widetilde{G}_P$, and G_P must satisfy, up to discretization errors, the relation

$$2M_N G_A(Q^2) - \frac{Q^2}{2M_N}\widetilde{G}_P(Q^2) = 2\widehat{m}G_P(Q^2)\,, \tag{12}$$

on each ensemble. All pre Ref. [36] calculations did not check this relation and missed observing that the data showed large deviations. Calculations subsequent to Ref. [39] that include the lowest mass gap state, $N(\mathbf{p}=1)\pi(\mathbf{p}=-1)$, in the analysis, obtain form factors that satisfy PCAC to within $\approx 10\%$ already at lattice spacing of $a \approx 0.9$ fm. (The ETMC result is an exception as explained in Ref. [23]). An illustration of the size of the deviation from unity of $R_1+R_2 \equiv \frac{2\widehat{m}G_P(Q^2)}{M_N G_A(Q^2)} + \frac{Q^2\widetilde{G}_P(Q^2)}{4M_N^2 G)_A(Q^2)}$, without and with the lowest $N\pi$ state included is shown in Fig. 5 taken from Ref. [19].

To summarize, satisfying the PCAC relation in Eq. (12) provides a strong and necessary constraint on the extraction of the three axial form factors. χPT analysis by Bär [37, 38] and data driven validation in Ref. [29, 31, 39] show that the lowest, $N(\mathbf{p}=1)\pi(\mathbf{p}=-1)$ and $N(\mathbf{p}=0)\pi(\mathbf{p}=1)$, states makes a large contribution on the two sides, respectively, and need to be included in the analysis. For percent level precision, the next question is—what other states need to be included? Current analyses include up to three states, where the third state, if its parameters are left free, effectively tries to account for all residual ESC. Such fits have been implemented in different ways.

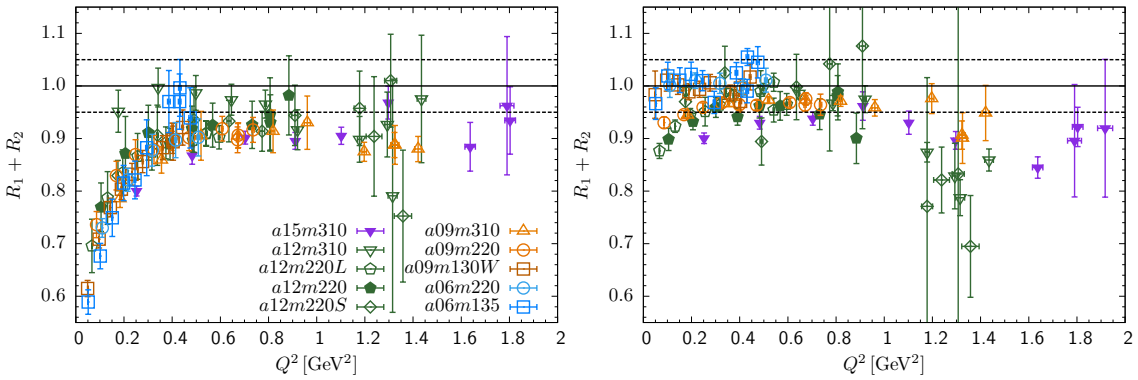

Figure 5: (Left) Results for $R_1 + R_2$ on 10 ensembles from fits to C_J^{3pt} without including the $N\pi$ state, i.e., the spectrum taken from fits to C^{2pt}. (Right) Including the $N\pi$ state. For PCAC to be satisfied, $R_1 + R_2$ should be unity up to discretization errors. The dotted lines show the 5% deviation band.

For example, in Ref. [29], the $N\pi$ state is hardwired and the third state is taken to be the lowest excited state in fits to C^{2pt}. In Refs. [19, 27, 39], a simultaneous fit to all five $J = A_\mu$ and P correlators is made wherein the A_4 correlator fixes E_1 to approximately the non-interacting energy of the $N\pi$ state. Over time, with much higher statistics data, results from different collaborations using different methods should converge as more more excited states are included.

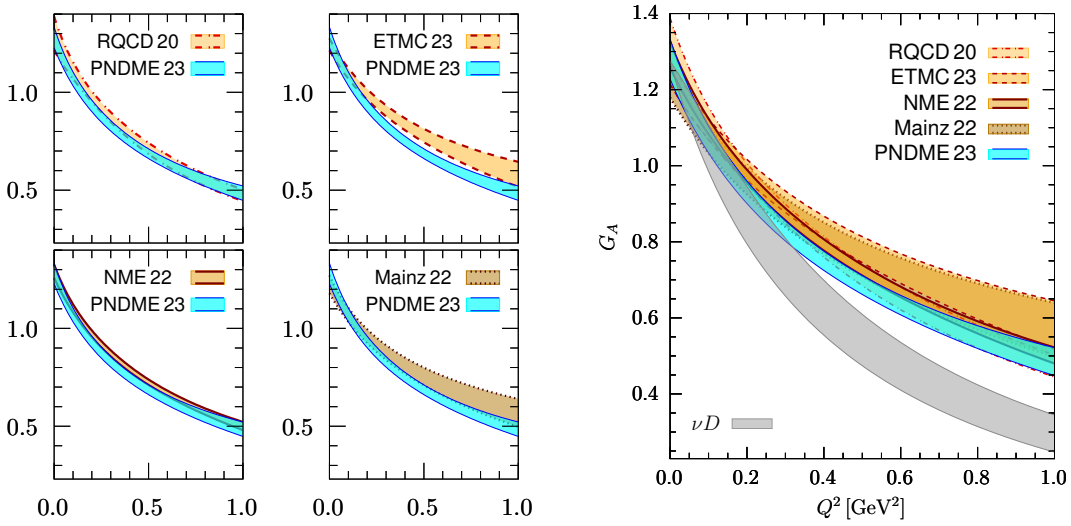

Figure 6: (Left) Comparison of the nucleon axial-vector form factor $G_A\left(Q^2\right)$ as a function of Q^2, the momentum transfer squared, obtained by the PNDME 23 [19] shown by the turquoise band; RQCD 19 [29] (light faun band); ETMC 21 [23] (faun band); NME 22 [27] (light brown band); and Mainz 22 [26] (brown band). The νD band is the fit to the old neutrino-deuterium data taken from Ref. [20].

2.5 Extrapolating lattice AVFF to the physical point for use in phenomenology

The next step, once ESC have been removed and form factors have been extracted from GSME on each ensemble, is to extrapolate these data to the physical point and provide a parameterized form for G_A and $\widetilde{G}_P$ that can be used in phenomenology. The challenge is that the discrete set of Q_i^2 values at which data are obtained are different on each ensemble.

One, simple to implement, way consists of the following three steps:

1. Parameterize the $G_A(Q_i^2)$ data on each ensemble. Depending on the number of Q_i^2 values, it could be a suitably truncated z-expansion or a Padé. The expected $1/Q^4$ asymptotic behavior can be built in by using sum rules in the z-expansion [40] or through an $\{n, n+2\}$ Padé in Q^2/M_N^2. The Mainz collaboration [26] combines the removal of ESC at various values of Q_i^2 and the Q^2 parameterization on a given ensemble to include correlations.

2. Pick n values of momenta, Q_k^2, over a range, say $0 \le Q^2 \le 1$ GeV^2. Extrapolate the data at each of these values of Q_k^2 using a simultaneous fit in $\{m_q, a, M_\pi L\}$ to the physical point. A typical ansatz used for such chiral-continuum-finite-volume (CCFV) extrapolations is

$$g(M_\pi, a, M_\pi L) = g_0 + c_1 a + c_2 M_\pi^2 + \frac{c_3 M_\pi^2 \exp(-M_\pi L)}{\sqrt{M_\pi L}}, \tag{13}$$

   where I have kept only the lowest order corrections in each of the $\{m_q, a, M_\pi L\}$ variables and assumed that discretization errors start at $O(a)$.

3. Having obtained the form factor in the continuum limit at the n points, Q_k^2, carry out the final parameterization, using again a truncated z-expansion or a Padé.

This 3-step process can be done within a single bootstrap procedure to propagate errors as has been done in Ref. [19, 27] to produce the NME and PNDME results shown in Fig. 6. Or these steps can be combined, especially if there are correlations between them. For example, to account for correlations between the coefficients of the CCFV fits at different values of Q_k^2 in step 2.

The plots in Fig. 6 provide two comparisons. In panels on the left, physical point results from the RQCD [24, 29], ETMC [23], NME [27], and Mainz [26] collaborations are compared against those from PNDME [19]. On the right they are overlaid and compared to the phenomenological extraction from the old neutrino-deuterium bubble chamber data [20]. The PNDME, RQCD and NME data mostly overlap, whereas the ETMC and Mainz data overlap and fall off slightly slower for $Q^2 \gtrsim 0.3$ GeV^2. On the other hand, the neutrino-deuterium (νD) data [20] falls off much faster for $Q^2 \gtrsim 0.2$ GeV^2. Overall, as shown in the right plot, the five lattice QCD estimates are consistent within 1σ and lie about 2σ above the νD band for $Q^2 \gtrsim 0.3$ GeV^2.

There also are results from CalLAT [16, 41], PACS [25, 42], and LHP+RBC+UKQCD [43] collaborations, which have not been included in the comparison because they have not been extrapolated to the physical point. The Fermilab collaboration [32] has embarked on the much harder problem of calculating transition matrix elements as well, e.g., $N \to \Delta$ or $N \to N\pi$.

From the analysis of the NME and PNDME data, my understanding is that the differences in exactly how the ESC are handled by the various collaborations and the consequent uncertainty in the final results should be considered work in progress. The uncertainty from the differences in the overall procedure for parameterization and CCFV extrapolation is, I believe, smaller because the data do not show large dependence on any of the three parameters $\{m_q, a, M_\pi L\}$, especially for $a \lesssim 0.1$ fm and $M_\pi L \gtrsim 4$, as illustrated in Fig. 7 [19, 27]. Hopefully, the next generation calculations will shed light on, and possibly resolve, the various differences.

Other findings in Refs. [19, 27] are (i) the dipole ansatz $G_A(Q^2) = \frac{g_A}{(1+cQ^2/M_N^2)^2}$ gives poor fits (very low p values) to data on many ensembles. Our conclusion, therefore, is that the lattice data

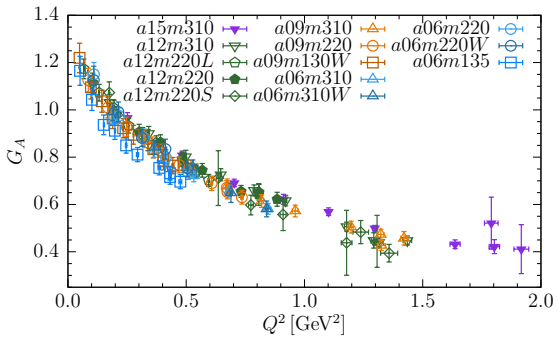

Figure 7: The data for renormalized $G_A(Q^2)$ on 13 HISQ ensembles show small variation in $\{a, M_\pi, M_\pi L\}$. The $a06m135$ data are statistics limited. Figure reproduced from Ref. [19].

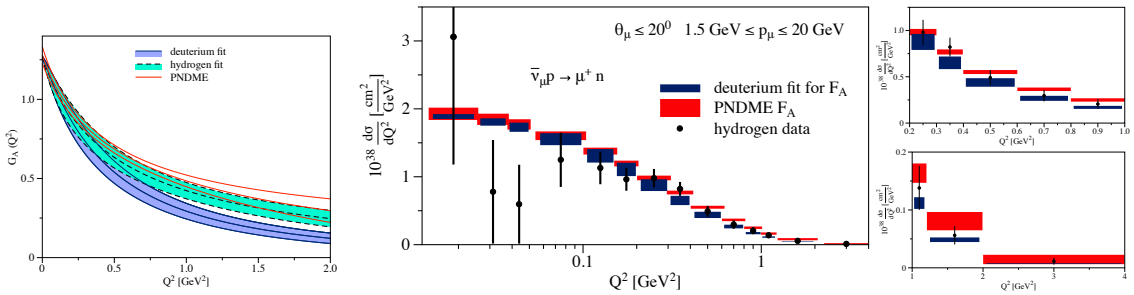

Figure 8: (Left) Comparison of the parameterized nucleon axial-vector form factor $G_A(Q^2)$ versus Q^2 up to 2 GeV^2 obtained from (i) fit to the deuterium bubble-chamber data [20] shown by blue solid lines with error band; (ii) fit to recent MINERvA antineutrino-hydrogen data [17], shown by black dashed lines and turquoise error band; and (iii) lattice QCD result obtained by the PNDME Collaboration [19] shown by red solid lines *without a band*. (Right) A comparison of antineutrino-nucleon charged current elastic differential cross section using AFF from (i) lattice QCD by the PNDME collaboration [19] (red bands) and (ii) the deuterium bubble-chamber data [20] (black bands) with the MINERvA antineutrino-hydrogen data [17] (black circles). These figures are taken from Ref. [18].

already show that the dipole ansatz does not have enough parameters to capture the Q^2 behavior over the range $0 \le Q^2 \le 1$ GeV^2. (ii) The PPD relation between G_A and $\widetilde{G}_P$ works very well.

2.6 Consistency check in the extraction of the axial charge g_A^{u-d}

There are two ways in which one can extract the axial charge g_A^{u-d}. The first is from the forward matrix element using C_{A_3} in Eq. (8) with $\boldsymbol{q} = 0$ and the second is by extrapolating the form factor $G_A(Q^2 \neq 0)$ to $Q^2 = 0$. I am considering them as separate because the extraction from the forward matrix element is computationally clean: $C_{A_3}(\boldsymbol{q} = 0)$ has the smallest errors and verification of the symmetry of the data about $\tau/2$ is a good test. The errors grow with $\boldsymbol{q}$ as shown in Fig. 2. On the other hand, $G_A(Q^2)$ is constrained by being part of the PCAC relation, Eq. (12), that has to be satisfied. The two results must agree after CCFV extrapolation. Based on the data in Ref. [19], I conclude

- The difference between g_A^{u-d} extracted without and with including $N\pi$ states is $O(\approx 6\%)$, i.e., 1.218(39) $\longrightarrow$ 1.294(48) on including one (the lowest) $N\pi$ state in the analysis. Note that the errors in each result are $O(\approx 3\%)$.

- The difference between $g_A^{u-d} \equiv G_A(Q^2 \to 0)$ extracted by extrapolating $G_A(Q^2)$ data obtained without and with including the lowest $N\pi$ state is also $O(\approx 6\%)$, i.e., $1.213(39) \to 1.289(56)$. Again, the errors in each are $O(\approx 4\%)$.

Thus, for each of the two cases, without and with $N\pi$ states, we get consistent estimates for g_A^{u-d} from the two methods, however results including the $N\pi$ state are about 6% larger. This difference is consistent with the expected $\sim 5\%$ 1-loop correction to the charge in χPT, however, it is roughly one combined σ. It therefore needs validation. My pick for the final result is the analysis including the $N\pi$ state since it gives form factors that satisfy the PCAC relation. Higher precision data are needed to further clarify the other significant ESCs and how to include them.

Collaboration	g_A^{u-d}	$\langle r_A^2 \rangle$ fm^2	g_P^*	$g_{\pi NN}$
PNDME 23	1.292(53)(24)	0.439(56)(34)	9.03(47)(42)	14.14(81)(85)
RQCD 19/23	1.284^{28}_{27}	0.449(88)	8.68(45)	12.93(80)
ETMC 23	1.283(22)	0.339(46)(6)	8.99(39)(49)	13.25(67)(69)
PACS 23	1.264(14)(1)	0.316(67)		
Mainz 22	1.225(39)(25)	0.370(63)(16)		
NME 21	1.32(6)(5)	0.428(53)(30)	7.9(7)(9)	12.4(1.2)
CalLat 18	1.271(10)(7)			
PNDME 18	1.218(25)(30)			
Mainz 19	$1.242(25)(^{0}_{-30})$			
χQCD 18	1.254(16)(30)			

Table 1: Comparison of g_A, $\langle r_A^2 \rangle$, g_P^* and $g_{\pi NN}$ from recent calculations: PNDME 23 [19], RQCD 19/23 [24, 29], ETMC 23 [28], PACS 23 [25, 42], Mainz 22 [26], and NME 21 [27]. Lattice results for all charges are usually quoted in the $\overline{\text{MS}}$ scheme at scale 2 GeV, however, note that the renormalization of g_A^{u-d} is trivial [21]. Earlier results for g_A^{u-d} with 2+1+1-flavor simulations by CalLat 18 [44] and PNDME 18 [45], and with 2+1-flavor simulations by Mainz 19 [46] and χQCD 18 [47] that entered in the averages compiled in the FLAG report 2021 [21] are given below the dividing line.

3. Comparison of charges obtained by various lattice collaborations

The results for the axial charge, g_A^{u-d}, the charge radius squared, $\langle r_A^2 \rangle$, the induced pseudoscalar coupling g_P^*, and the pion-nucleon coupling $g_{\pi NN}$, extracted from G_A and $\widetilde{G}_P$ by various collaborations using the relations

$$G_A(Q^2) = g_A(1 - \frac{\langle r_A^2 \rangle}{6} Q^2 + \cdots), \tag{14}$$

$$g_P^* \equiv \frac{m_\mu}{2M_N} \widetilde{G}_P(Q^{*2}), \tag{15}$$

$$g_{\pi NN} \equiv \lim_{Q^2 \to -M_\pi^2} \frac{M_\pi^2 + Q^2}{4M_N F_\pi} \widetilde{G}_P(Q^2). \tag{16}$$

are summarized in Table 1. Here m_μ is the muon mass and $Q^{*2} = 0.88 m_\mu^2$ is the energy scale of muon capture, and $F_\pi = 92.9$ MeV is the pion decay constant.

The results show about 10% variation in g_A^{u-d}, g_P^*, and $g_{\pi NN}$ and about 25% in $\langle r_A^2 \rangle$. Part of this is likely due to different methodologies used in the analysis, in particular how and if the lowest $N\pi$ state is included in the analysis. These results will improve steadily over time with higher statistics data.

4. Comparison of differential cross-section using lattice AVFF with MINERνA data

A comparison of the antineutrino-nucleon charged-current elastic cross sections calculated using predictions of AVFF from lattice (PNDME 23 [19]) and neutrino-deuterium analysis [20] with MINERvA measurement [17, 48] is presented in Fig. 8 reproduced from Ref. [18]. A χ^2 test was performed to determine the significance of the differences between the three. No significant difference was found between MINERvA-lattice QCD (PNDME) and between MINERvA-deuterium results. A $\approx 2.5\sigma$ tension was, however, found between the PNDME and the deuterium results. Based on data shown in Fig. 6, the deviation in the deuterium-Mainz and deuterium-ETMC will be even larger. To assess the scope for future progress, three regions of Q^2 with different prospects for the extraction of AVFF from lattice QCD and MINERvA-like experiments were identified.

For $Q^2 \lesssim 0.2$ GeV^2, LQCD predictions and fits to the deuterium bubble-chamber data are in good agreement. In this region, the experimental errors in the measurement on hydrogen by MINERvA are large, whereas the errors in the parameterization of the deuterium bubble chamber data are smaller. The νD result has often been used as a benchmark, however, note that there is unresolved uncertainty in the deuterium data as discussed in Ref. [20]. Also, no new deuterium data are expected in the near-term, so I do not comment on its future prospects. Lattice QCD data are competitive and will improve steadily. This region will be well-characterized by the axial charge, the axial charge radius, and well-parameterized by a low-order z-expansion or a Padé.

For 0.2 GeV$^2 \lesssim Q^2 \lesssim 1$ GeV^2, the AVFF from PNDME has the smallest errors and the predicted differential cross section lies above the hydrogen and νD values, i.e., the same ordering as for the AVFF shown in Fig. 8 (left). Future improvements in both the hydrogen data and lattice calculations will provide robust cross-checks in this region.

The region $Q^2 \lesssim 0.5$ GeV^2 is where lattice QCD data, even with current methodology, will improve rapidly as more simulations are done closer to $M_\pi = 135$ MeV, $a \to 0$ and on larger volumes because, in these limits and for given statistics, the value of $Q^2|_{\rm max}$ with a good signal (usually taken to be some fixed lattice momentum $\mathbf{n}^2$) decreases.

For $Q^2 \gtrsim 1$ GeV^2, current LQCD data have larger statistical errors and systematic uncertainties—discretization and residual excited state contributions. With the current methodology, the lattice AVFF comes mostly from simulations with $M_\pi \gtrsim 300$ MeV on $a < 0.1$ fm ensembles [19]. If the dependence on $\{a, M_\pi\}$ is mild, as has been observed so far, then these data are useful by themselves. With higher statistics and improved actions, one can push the lattice momenta $\boldsymbol{n}^2|_{\rm max}$ higher and perhaps reliably reach $Q^2 \sim 2$ GeV^2. Nevertheless, new methods are definitely needed to get data at $Q^2 \gtrsim 2$ GeV^2 from simulations with physical pion masses, $M_\pi \approx 135$ MeV and $a < 0.1$ fm. Similarly, improvements in MINERvA and follow on experiments are needed to cover the full range of Q^2 relevant for DUNE.

5. Concluding remarks

Extensive calculations of the AVFF are being carried out by at least the following nine lattice QCD collaborations: PNDME [19], RQCD [24, 29], ETMC [23], NME [27], Mainz [26], CalLAT [16, 41], PACS [25, 42], LHP+RBC+UKQCD [43], and Fermilab [32]. As shown in Sections 3 and 2.5, we now have results to within 10% precision. The major uncertainty comes from resolving and removing excited-state contributions.

The good news is that the methodology for the calculation of the correlation functions, C^{2pt} and C_J^{3pt}, is robust. The bad news is that the exponentially falling signal to noise ratio in them means that ESC are large at source-sink separations possible in today's calculations. Second, it is also clear that multihadron, $N\pi$, excited states give large contributions which must be removed. Unfortunately, it is not yet known how many of these states need to be included in the analysis for percent level precision. The operator constraint that the form factors satisfy the PCAC relation in Eq. (12) provides a valuable check, so it must be carried out in all calculations. The third challenge is getting data at large Q^2 because the discretization and statistical errors grow with Q^2 on a given ensemble. Also, the $Q^2|_{\rm max}$ (the largest lattice momenta $2\pi \boldsymbol{n}/La$ with a good signal to noise ratio for fixed statistics) decreases as simulations are done closer to the physical point. Thus, to get data for $Q^2 \gtrsim 1$ GeV^2 on physical pion mass ensembles will need/benefit from new methods and very high statistics.

As first step towards percent level precision, my estimate is that a factor of ten increase in statistics will reduce the statistical errors to a level that will provide much more clarity in removing ESC. Similary new developments, including variational methods [31] with multihadron states and momentum smearing [49], will improve the calculations and extend the range of Q^2. I anticipate continued improvements in both, statistics and methods, will provide LQCD predictions of AVFF for nucleons in the range $Q^2 \lesssim 2$ GeV^2 (hopefully higher) with percent level precision by about 2030, in concert with DUNE producing data.

Acknowledgments

Many thanks to my collaborators, Yong-Chull Jang, Sungwoo Park, Oleksandr Tomalak, Tanmoy Bhattacharya, Vincenzo Cirigliano, Huey-Wen Lin, Emanuele Mereghetti, Santanu Mondal, and Boram Yoon for making the PNDME and NME results happen. Also to all who presented relevant results at Lattice 2023 and to André Walker-Loud for valuable comments. Our calculations used the Chroma software suite [50] and resources at (i) the National Energy Research Scientific Computing Center, a DOE Office of Science User Facility supported by the Office of Science of the U.S. Department of Energy under Contract No. DE-AC02-05CH11231; (ii) the Oak Ridge Leadership Computing Facility, which is a DOE Office of Science User Facility supported under Contract DE-AC05-00OR22725, through awards under the ALCC program project LGT107 and INCITE award HEP133; (iii) the USQCD collaboration, which is funded by the Office of Science of the U.S. Department of Energy; and (iv) Institutional Computing at Los Alamos National Laboratory. R. Gupta was partly supported by the U.S. Department of Energy, Office of Science, Office of High Energy Physics under Contract No. DE-AC52-06NA25396 and by the LANL LDRD program.

References

[1] UCNA Collaboration collaboration, M. Mendenhall et al., *Phys.Rev.* **C87** (2013) 032501 [1210.7048].

[2] UCNA collaboration, M. A. P. Brown et al., *Phys. Rev.* **C97** (2018) 035505 [1712.00884].

[3] B. Märkisch et al., *Phys. Rev. Lett.* **122** (2019) 242501 [1812.04666].

[4] D. Mund, B. Maerkisch, M. Deissenroth, J. Krempel, M. Schumann, H. Abele et al., *Phys. Rev. Lett.* **110** (2013) 172502 [1204.0013].

[5] M. Ademollo and R. Gatto, *Phys.Rev.Lett.* **13** (1964) 264.

[6] J. F. Donoghue and D. Wyler, *Phys.Lett.* **B241** (1990) 243.

[7] T. Bhattacharya, V. Cirigliano, S. D. Cohen, A. Filipuzzi, M. Gonzalez-Alonso, M. L. Graesser et al., *Phys. Rev. D* **85** (2012) 054512 [1110.6448].

[8] A. N. Ivanov, M. Pitschmann, N. I. Troitskaya and Y. A. Berdnikov, *Phys. Rev. C* **89** (2014) 055502 [1401.7809].

[9] A. Czarnecki, W. J. Marciano and A. Sirlin, *Phys. Rev. Lett.* **120** (2018) 202002.

[10] A. Czarnecki, W. J. Marciano and A. Sirlin, *Phys. Rev.* **D100** (2019) 073008 [1907.06737].

[11] A. Czarnecki, W. J. Marciano and A. Sirlin, *Phys. Rev.* **D101** (2020) 091301 [1911.04685].

[12] M. Horoi and A. Neacsu, *Phys. Rev. C* **98** (2018) 035502 [1801.04496].

[13] B. W. Carroll and D. A. Ostlie, 2007.

[14] L. Alvarez Ruso et al., 2203.09030.

[15] USQCD collaboration, A. S. Kronfeld, D. G. Richards, W. Detmold, R. Gupta, H.-W. Lin, K.-F. Liu et al., *Eur. Phys. J.* **A55** (2019) 196 [1904.09931].

[16] A. S. Meyer, A. Walker-Loud and C. Wilkinson, *Ann. Rev. Nucl. Part. Sci.* **72** (2022) 205 [2201.01839].

[17] MINERvA collaboration, T. Cai et al., *Nature* **614** (2023) 48.

[18] O. Tomalak, R. Gupta and T. Bhattacharya, *Phys. Rev. D* **108** (2023) 074514 [2307.14920].

[19] Precision Neutron Decay Matrix Elements (PNDME) collaboration, Y.-C. Jang, R. Gupta, T. Bhattacharya, B. Yoon and H.-W. Lin, *Phys. Rev. D* **109** (2024) 014503 [2305.11330].

[20] A. S. Meyer, M. Betancourt, R. Gran and R. J. Hill, *Phys. Rev. D* **93** (2016) 113015 [1603.03048].

[21] Flavour Lattice Averaging Group (FLAG) collaboration, Y. Aoki et al., *Eur. Phys. J. C* **82** (2022) 869 [2111.09849].

[22] Flavour Lattice Averaging Group collaboration, S. Aoki et al., *Eur. Phys. J. C* **80** (2020) 113 [1902.08191].

[23] C. Alexandrou, S. Bacchio, M. Constantinou, J. Finkenrath, R. Frezzotti, B. Kostrzewa et al., 2309.05774.

[24] G. S. Bali, S. Collins, S. Heybrock, M. Löffler, R. Rödl, W. Söldner et al., 2305.04717.

[25] PACS collaboration, R. Tsuji, N. Tsukamoto, Y. Aoki, K.-I. Ishikawa, Y. Kuramashi, S. Sasaki et al., *Phys. Rev. D* **106** (2022) 094505 [2207.11914].

[26] D. Djukanovic, G. von Hippel, J. Koponen, H. B. Meyer, K. Ottnad, T. Schulz et al., *Phys. Rev. D* **106** (2022) 074503 [2207.03440].

[27] Nucleon Matrix Elements (NME) collaboration, S. Park, R. Gupta, B. Yoon, S. Mondal,

T. Bhattacharya, Y.-C. Jang et al., *Phys. Rev. D* **105** (2022) 054505 [2103.05599].
[28] C. Alexandrou et al., *Phys. Rev. D* **103** (2021) 034509 [2011.13342].
[29] RQCD collaboration, G. S. Bali, L. Barca, S. Collins, M. Gruber, M. Löffler, A. Schäfer et al., *JHEP* **05** (2020) 126 [1911.13150].
[30] R. Babich, J. Brannick, R. C. Brower, M. A. Clark, T. A. Manteuffel, S. F. McCormick et al., *Phys. Rev. Lett.* **105** (2010) 201602 [1005.3043].
[31] L. Barca, G. Bali and S. Collins, *Phys. Rev. D* **107** (2023) L051505 [2211.12278].
[32] A. V. Grebe and M. Wagman, 2312.00321.
[33] S. Gusken, U. Low, K. H. Mutter, R. Sommer, A. Patel and K. Schilling, *Phys. Lett. B* **227** (1989) 266.
[34] G. Parisi, *Phys. Rept.* **103** (1984) 203.
[35] G. P. Lepage, in *Boulder ASI 1989:97-120*, pp. 97–120, 1989, http://alice.cern.ch/format/showfull?sysnb=0117836.
[36] R. Gupta, Y.-C. Jang, H.-W. Lin, B. Yoon and T. Bhattacharya, *Phys. Rev.* **D96** (2017) 114503 [1705.06834].
[37] O. Bär, in *36th International Symposium on Lattice Field Theory (Lattice 2018) East Lansing, MI, United States, July 22-28, 2018*, 2018, 1808.08738.
[38] O. Bär, *Phys. Rev. D* **99** (2019) 054506 [1812.09191].
[39] Y.-C. Jang, R. Gupta, B. Yoon and T. Bhattacharya, *Phys. Rev. Lett.* **124** (2020) 072002 [1905.06470].
[40] G. Lee, J. R. Arrington and R. J. Hill, *Phys. Rev. D* **92** (2015) 013013 [1505.01489].
[41] A. S. Meyer et al., *PoS* **LATTICE2021** (2022) 081 [2111.06333].
[42] PACS collaboration, R. Tsuji, Y. Aoki, K.-I. Ishikawa, Y. Kuramashi, S. Sasaki, K. Sato et al., 2311.10345.
[43] LHP, RBC,, UKQCD collaboration, S. Ohta, in *40th International Symposium on Lattice Field Theory*, 11, 2023, 2311.05894.
[44] CalLat collaboration, C. C. Chang et al., *Nature* (2018) [1805.12130].
[45] R. Gupta, Y.-C. Jang, B. Yoon, H.-W. Lin, V. Cirigliano and T. Bhattacharya, *Phys. Rev.* **D98** (2018) 034503 [1806.09006].
[46] T. Harris, G. von Hippel, P. Junnarkar, H. B. Meyer, K. Ottnad, J. Wilhelm et al., *Phys. Rev. D* **100** (2019) 034513 [1905.01291].
[47] [χQCD 18] J. Liang, Y.-B. Yang, T. Draper, M. Gong and K.-F. Liu, *Phys. Rev.* **D98** (2018) 074505 [1806.08366].
[48] F. Irani, M. Goharipour, H. Hashamipour and K. Azizi, 6, 2023.
[49] G. S. Bali, B. Lang, B. U. Musch and A. Schäfer, *Phys. Rev. D* **93** (2016) 094515 [1602.05525].
[50] SciDAC Collaboration, LHPC Collaboration, UKQCD Collaboration collaboration, R. G. Edwards and B. Joo, *Nucl.Phys.Proc.Suppl.* **140** (2005) 832 [hep-lat/0409003].